Chemical Engineering Journal 432 (2022) 134370

Contents lists available at ScienceDirect

Chemical Engineering Journal

journal homepage: www.elsevier.com/locate/cej

Moisture-resistant MXene-sodium alginate sponges with sustained superhydrophobicity for monitoring human activities

Yangchengyi Liu [a], Zhong Sheng [a], Jielong Huang [a], Weiyi Liu [a], Hongyan Ding [a], Jinfeng Peng [c], Bowen Zhong [a], Yuhui Sun [a], Xiaoping Ouyang [a], Huanyu Cheng [b,*], Xiufeng Wang [a,*]

[a] School of Materials Science and Engineering, Xiangtan University, Xiangtan, Hunan 411105, PR China
[b] Department of Engineering Science and Mechanics, The Pennsylvania State University, University Park, PA 16802, USA
[c] School of Mechanical Engineering, Xiangtan University, Xiangtan, Hunan 411105, PR China

ARTICLE INFO

Keywords:
MXene-sodium alginate sponges
Joule heating
Sustained superhydrophobicity
Moisture-resistant
Monitoring of human activities

ABSTRACT

Wearable mechanical sensors are susceptible to moisture, causing inaccuracy for monitoring human health and body motions. Although the superhydrophobic barrier on the sensor surface has been extensively explored as a passive water repel strategy, the dense superhydrophobic surface often has limited flexibility and inevitably degradates in high humidity or saturated water vapor environments due to the nucleation and growth of small size water molecules. This work reports a superhydrophobic MXene-sodium alginate sponge (SMSS) pressure sensor with efficient low-voltage Joule heating to provide sustained superhydrophobicity for moisture-resistant sensing. The superhydrophobic surface on the outside can repel large size water droplets, whereas the Joule heating efficiently removes small size water droplets and significantly reduces water molecule adsorption throughout the sponge. Because of the sustained superhydrophobic barrier and high porosity in the sponge, the SMSS pressure sensor with high sensitivity, large sensing range, and quick response can accurately and reliably function and monitor varying biophysical signals even in extreme use scenarios with high humidity or water vapor environments.

1. Introduction

Among various wearable devices to detect human motions and health status, the piezoresistive pressure sensors that can transduce mechanical excitation into readable electrical signals are widely explored due to their simple structure and low-cost fabricate process [1–3]. The higher-performance piezoresistive pressure sensors often rely on the exploration of microstructures (e.g., porous or hollow [4,5], micro-pyramidal [6,7], or interlocked microstructure [8,9]) and/or functional materials (e.g., graphene [10], MXene [11,12], carbon nanotubes [13,14], metal nanostructures [15], carbon black [16], and conducting polymers [17]). MXene is a promising candidate for advanced pressure sensors due to its 2D structure, high electrical conductivity, hydrophilic surface, and ease of processing, and thus can be utilized in the strain sensor, humidity sensor, fire warning sensor et al [18–21]. However, the hydrophilic surface is susceptible to moisture and hampers electron transport, resulting in increased electrical resistance [22,23]. The moisture can come from both the human body (e.g., sweat [24], transepidermal water loss, breath, and wound drainage) and the external environment (e.g., rain droplets and fog vapor).

In order to avoid electronic sensing interference and maintain desirable service life, superhydrophobic modification has been proposed to minimize the water interference for the wearable sensor [25–29]. As few contact area exists between the water droplets and superhydrophobic surface, it is difficult for water molecules to permeate into the conductive layer of the sensor [21,30]. Many works exsit for superhydrophobic MXene, MXene/alginate composites, MXene with Joule heating, and MXene for human activities monitoring. These strategies can insulate the sensing materials from water molecules in humid environments [31–33]. For example, the octadecyl isocyanate modified TiO_2 nanoparticle coating with a nanosized porous structure deposited on the hydrophilic PEDOT: PSS conductive layer can prevent the water molecules penetration and humid interference [33]. Moreover, the combination of hemisphere arrays and CNT constructs a surface hierarchical micro-/nano- structure to inhibit the water vapor condensation inside the conductive networks [32]. Although these strategies can

* Corresponding authors.
E-mail addresses: Huanyu.Cheng@psu.edu (H. Cheng), onexf@xtu.edu.cn (X. Wang).

https://doi.org/10.1016/j.cej.2021.134370
Received 16 October 2021; Received in revised form 14 December 2021; Accepted 23 December 2021
Available online 28 December 2021

isolate the conductive materials from the humid environments to partially provide humid-insensitivity under the static state (i.e., without pressure cycles), their dynamic sensing performance (critical for practical applications) under high humidity is seldom reported. It is worth noting that the dynamic pressure cycles often cause deformation and cracking in the superhydrophobic coating to result in performance degradation. Because of the crack generation [34] and water molecules condensation [35], the dense superhydrophobic surface is difficult to ensure a stable isolation effect during dynamic deformation under high humidity conditions. In fact, another recent report indicates that the superhydrophobic collagen-based pressure sensor (in 82 % RH and 50 ℃) shows a much higher relative resistance change [36]. Moreover, the degenerated superhydrophobic surface is no longer waterproof and easily wetted in the external high humidity environments to result in further performance degradation. This phenomenon has often been ignored in superhydrophobic wearable sensors [37]. Therefore, an effective strategy to prevent the nucleation and condensation of water molecules on the sensor surface is highly desirable to provide sustained superhydrophobicity for moisture-insensitive sensing, especially in high humidity and saturated water vapor conditions.

Common condensation-resistant superhydrophobic surfaces have been demonstrated (e.g. nanotexturing through droplet coalescence, scaling the texture to prevent filling, and minimizing the adhesion force) [32,38,39]. However, all of these approaches fail to prevent the initial nucleation of water molecules that are smaller than the microstructures of the superhydrophobic surface [40]. Joule heating that converts the electrical energy into thermal energy has been widely used in many applications, including thermotherapy [23], strain monitoring [41], thermal alarming [42], and thermal management [43]. By the high temperature-driven water evaporation, the Joule heating effect would be a promising strategy to avoid moisture interference caused by absorption of water molecules for sustained superhydrophobicity and stable sensing. Though the porous structure of the sponge can provide lightweight and high-performance sensors, the high surface area would cause easier water accumulation compared to the sensors without porous structure, creating faster and more severe degradation in superhydrophobicity and resulting sensor performance [44]. Therefore, it is highly desirable to develop strategies to achieve the sustained superhydrophobicity and robust sensing during the static and dynamic processes.

To address these challenges, this work reports a superhydrophobic MXene-sodium alginate sponge (SMSS) with excellent Joule heating to provide sustained superhydrophobicity and reliable sensing performance in a humid environment even upon large mechanical deformation. The nearly unchanged contact angle in saturated water vapor for 20 min supports the stability of the superhydrophobic surface for sustained superhydrophobicity. The sensing performance variation of our SMSS pressure sensor with Joule heating improves ~ 9.4 times (4.3% vs. 40.4 % of without heating) in 70% relative humidity (RH) and ~ 23.7 times (8.96% vs. 212.37% of without heating) in saturated water vapor under more than 85 dynamic pressure cycles. Meanwhile, the stability of the superhydrophobic layer is also improved in saturated water vapor conditions by Joule heating (20 min without obvious change of contact angle) to provide sustained waterproof property. As a result, the SMSS pressure sensors with high sensitivity and large sensing range as well as moisture-resistant performance can reliably detect various human motions in all-weather conditions. The design and demonstration of our SMSS sensor provide a versatile platform to enable sustained superhydrophobicity and robust sensing performance for the next-generation stretchable epidermal sensors to be used in highly humid or water vapor conditions.

2. Results and discussions

2.1. Fabrication process of the SMSS

The fabrication process of the SMSS starts with the dip-coating of MXene-SA, followed by spray-coating of the hydrophobic fumed silica (Hf-SiO_2) nanoparticles (Fig. 1**a**). In brief, the $Ti_3C_2T_x$ nanosheets were first prepared by selectively etching the Al element from the Ti_3AlC_2 MAX phase using lithium fluoride/hydrochloric acid (LiF/HCl) solution, as confirmed by the disappeared 104 peaks (~39°) in the $Ti_3C_2T_x$ MXene (**Fig. S1 a**). The X-ray diffraction (XRD) also shows the downshift of the 002 peak from 9.52° to 6.06° after etching, due to the expanded interplanar spacing between the MXene sheets from the introduced functional groups and water. The very thin MXene nanosheets are also observed in the cross-sectional scanning electron microscope (SEM) and the atomic force microscope (AFM) image (**Fig. S1 b,c**), which is consistent with previous reports [45]. The resulting MXene film shows excellent flexibility and the strong Tyndall effect from the as-prepared MXene nanosheets suspension indicates good uniformity and stability (**Fig. S1 d**). Next, the sodium alginate (SA) powders were added dropwise into the MXene suspension under continuous stirring to produce a homogeneous MXene-SA suspension, exhibiting long-term stability without precipitation after a month (**Fig. S2**). The immersion of the commercial melamine–formaldehyde (MF) sponges cut into 1.5 × 1.5 × 1.5 cm^3 cubes in the MXene-SA suspension was followed by drying in vacuum degassing to ensure robust adhesion. This dipping-and-drying process was repeated four times to increase the thickness in the coated MXene-SA for enhanced conductivity by two orders of magnitude (**Fig. S3 a**). The comparison in the SEM images before (Fig. 1**c, top**) and after the coating with MXene-SA composites (Fig. 1**d, top**) shows unchanged connected porous structures in the sponge. A continuous layer of overlapped MXene-SA on the smooth MF framework is confirmed by the magnified SEM images (Fig. 1**c, d, bottom**) and Energy-dispersive X-ray spectroscopy (EDS) elemental mapping images (**Fig. S5**). To obtain the waterproof functions, the superhydrophobic surface was constructed on the sensor by spray-coating Hf-SiO_2 nanoparticles on the 3D frameworks (without subsequent chemical modification). Compared with the other methods such as dip-coating, electrospinning, lithography, and chemical vapor deposition of varying materials, the chosen approach is simple, efficient, and scalable [46]. Through spray-coating, the Hf-SiO_2 nanoparticles anchored on the outer layer of MXene-SA framework via Van der Waals interactions (**Fig. S5**) contribute to the considerably increased roughness (Fig. 1**e, bottom**). The as-prepared SMSS sponge cubes can be placed on the floret of a Camellia flower head without obvious deformation to show its lightweight (Fig. 1**b**). Notably, the presence of the SA molecule as a hydrogen bonding agent could improve the mechanical property of the MXene-SA coating due to numerous oxygen-containing polar groups (–OH, $–COO^-$, and = O), while maintaining excellent electrical conductivity compared with the other alternative polymers (e.g., polysaccharides, PAM, PAA) [47,48]. The slight redshift and intensity decrease of the 002 peaks in the XRD patterns (Fig. 1**f**) indicates the expanded interlayer spacing of MXene from the insertion of SA molecules and increases the disorder between MXene nanosheets [50]. The comparison in the Fourier transforms infrared (FTIR, Fig. 1**g**) spectra also shows a new absorption peak (1596 cm^{-1}) in the MXene-SA framework, corresponding to the antisymmetric stretching vibration mode of the $–COO^-$. The redshift from 3459 cm^{-1} to 3430 cm^{-1} in the peak for the –OH stretching vibration also implies the possible formation of enhanced hydrogen bonding between SA molecules and MXene nanosheets. The comparison of X-ray photoelectron spectroscopy (XPS) spectra between MXene and MXene-SA sheets shows stronger C-O and O-C = O peaks and confirms the valence change of MXene after SA binding (**Figure S6**) [49]. The MXene with SA could provide a more uniform coating (Fig. 1**h,** inset) and higher electrical conductivity (Fig. 1**h**) than that without SA, as evidenced by the high-magnification SEM image of the MF skeleton wrapped by MXene

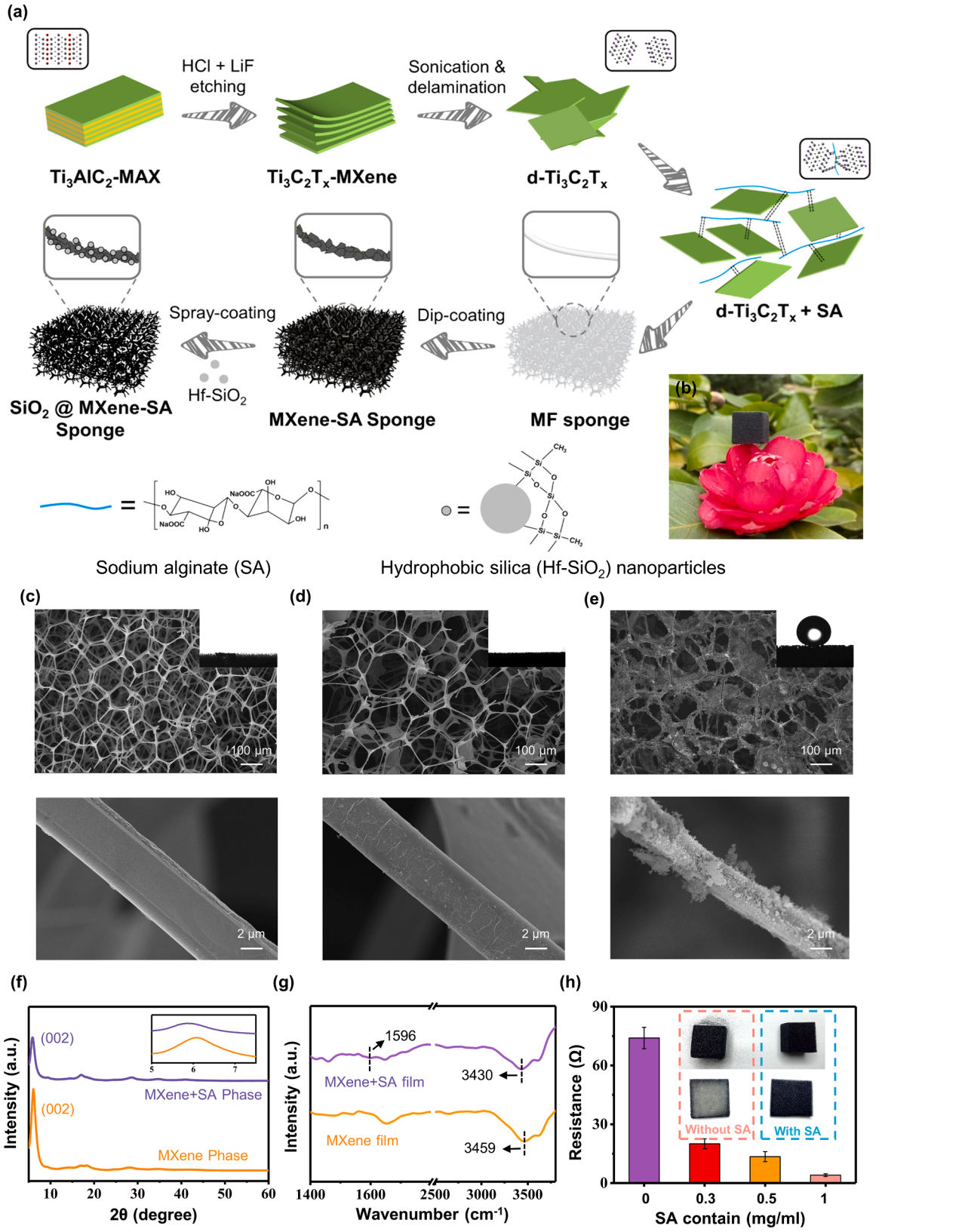

Fig. 1. Fabrication and characterization of the SMSS. (a) Schematic diagram of the fabrication process of the SMSS to show the preparation of MXene-SA dispersion and its dip-coating on the melamine–formaldehyde (MF) sponge framework, followed by spray-coating of Hf-SiO_2 nanoparticles. (b) Photograph of the lightweight SMSS on the red flower without deformation. (c-e) Scanning electron microscopy (SEM) images of the MF sponges (c) before and after coating of (d) MXene-SA and (e) Hf-SiO_2, with magnified views shown at the bottom. The insets are contact angle images of a water droplet upon correspopnding sponge cubes, with the CA increased from 0° (c, d) to 158.2° (e). (f) XRD patterns of the MXene and MXene-SA sheets with a magnified view are shown in the inset. (g) FTIR spectra of the MXene and MXene-SA sheets. (h) Comparisons of electrical resistances of SMSS with different SA content after 4 times dip-coating (0 %, 0.3 %, and 0.5 %). Inset: photographs of MXene and MXene-SA sponges after 1000 compression cycles, with their cross-sectional views shown at the bottom.

(**Figure S7**) and the comparison with the SEM image of the MXene-SA sponge (Fig. 1**d**). This is attributed to the oxygen-containing polar groups in the SA molecules for enhanced interaction between the polar group of MXene nanosheets and the amino groups on the sponges. Moreover, compared to the obvious shedding in the MXene sponge without SA, the MXene sponge with SA remains intact after 1000 compression cycles (Fig. 1**h,** inset).

2.2. Robust superhydrophobicity of the SMSS

The superhydrophobic surface of the SMSS fabricated by simple and scalable spray coating can effectively repel a broad range of probe liquids with different surface tensions (e.g., water, sweat, tea, coffee, milk, and juice), as evidenced by the spherical droplets shown in Fig. 2**a**. Notably, the contact angle (CA) of sweat on the SMSS surface 152.3° is slightly smaller than that of water (158.2°) due to the skin lipids in sweat and changed surface tension. The superhydrophobic surface against water and sweat remains stable for more than a month (**Fig. S8**). The low-adhesion property of the surface to water droplet leaves no trace of water on the surface as the droplet at the pipette tip moves away from the surface (Fig. 2**b, top**). The water droplet also quickly rolls off from the surface with a rather tiny tilting angle ~ 3.5° (Fig. 2**b, bottom**). In addition, the superhydrophobic surface is mechanically durable against tape-peeling, extrusion, and corrosion as shown in Fig. 2**c-e**. Specifically, the SMSS under repeated tape-peeling for 100 times does not change the CA (greater than 150° for both water and sweat in Fig. 2**c**). The repeated squeezing between 0 and 80 % compressive strain in the extrusion test also results in a negligibly small change from 157.2° to 155.7° in the CA (Fig. 2**d**). The CA of SMSS remains almost unchanged when it is immersed into acid (pH = 3), neutral (pH = 7), or alkaline

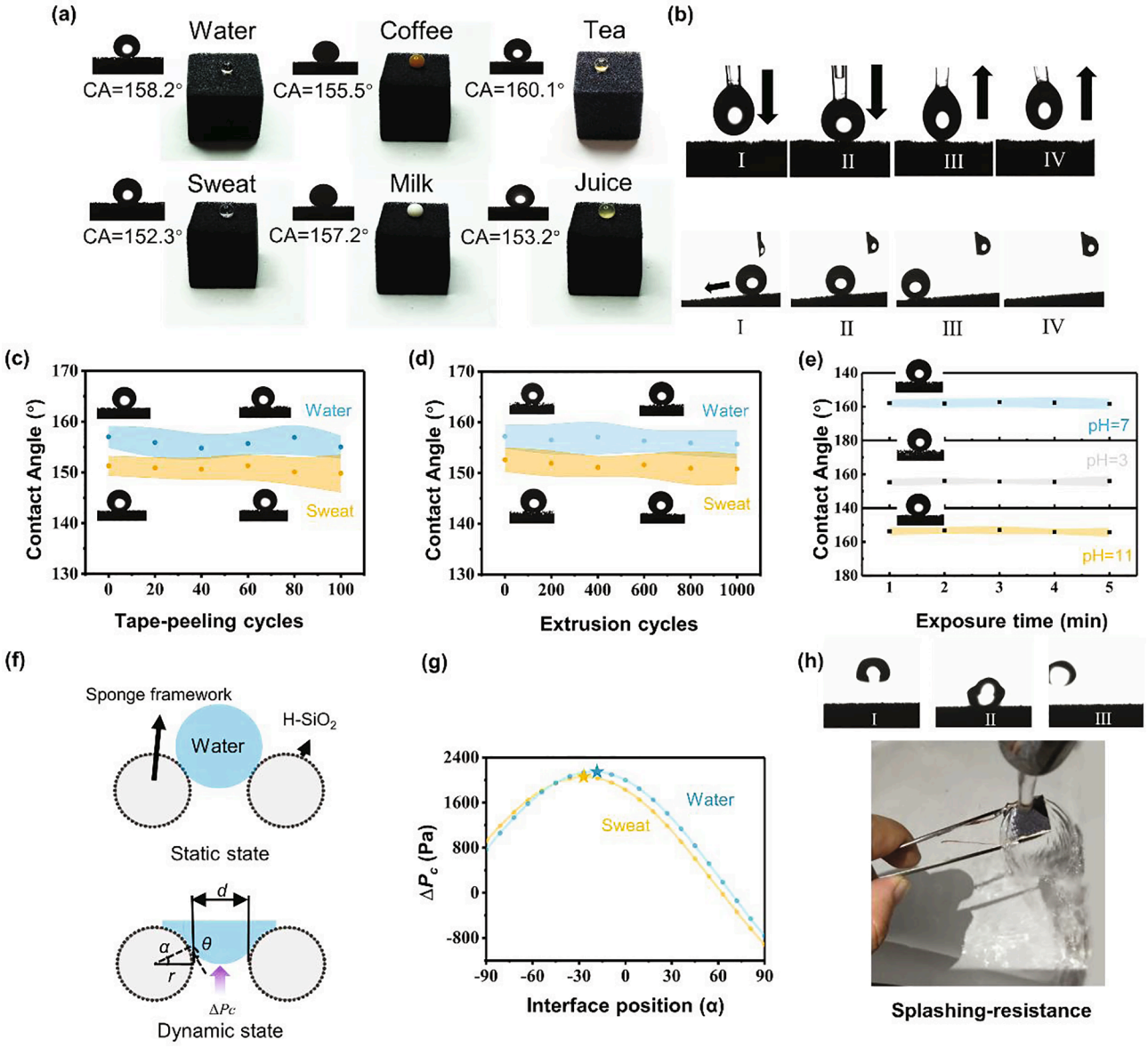

Fig. 2. Superhydrophobic performance of the SMSS. (a) Liquids with different surface tensions (i.e., water, sweat, tea, coffee, milk, and juice) on the SMSS and CA data. (b) Photographs to show the low adhesion between the SMSS and water droplets. The CA of the water droplet on the SMSS as a function of (c) tape-peeling and (d) extrusion cycles, as well as (e) immersion time of the SMSS in different pH environments (pH = 3, 7, and 11). The inset images are contact angle images of a water droplet upon SMSS during tape-peeling, extrusion, and corrosion cycles. (f) Schematic diagrams to show the static and dynamic water droplets on the superhydrophobic SMSS surface. (g) Determination of the critical bursting pressure from the curve of the bursting pressure as a function of the position of the air–liquid interface (between the porous structure in SMSS and water or sweat). (h) Dynamic wetting tests on the SMSS surface show droplet bouncing (top) and water spreading away from the surface (bottom).

(pH = 11) solutions for more than 5 min (Fig. 2**e**). The robustness of the superhydrophobic SMSS sponge in a static state is attributed to the combined micro-porous structure of the MF sponge, micro/nano-textured surface, and the Hf-SiO_2 nanoparticles (Fig. 2**f, top and** Figure S9). Besides the static state, the SMSS sponge also exhibits dynamic water-repellent property before the applied droplet pressure exceeds the critical bursting pressure (ΔP_c) (Fig. 2**f, bottom**). Based on the capillary theory, the bursting pressure for the sponge skeleton with radius r and spacing d can be estimated as $\Delta P = \frac{2\sigma\cos(\theta_{CA}-\alpha)}{d+r(1-\cos\alpha)}$, where α is liquid surface tension, θ_{CA} is the apparent contact angle, α is the position of the advancing front of the air–liquid interface. The sponge skeleton in this study has a radius of 5.8 μm (Fig. 1**e**) and a spacing of 133.78 μm measured by mercury intrusion porosimetry (Fig. S10). For water ($\sigma_{water} = 72$ mN/m, $\theta_{CA,\ water} = 158.2°$) and sweat ($\sigma_{sweat} = 69.1\,mN/m$, $\theta_{CA,\ sweat} = 152.3°$), the bursting pressure ΔP can

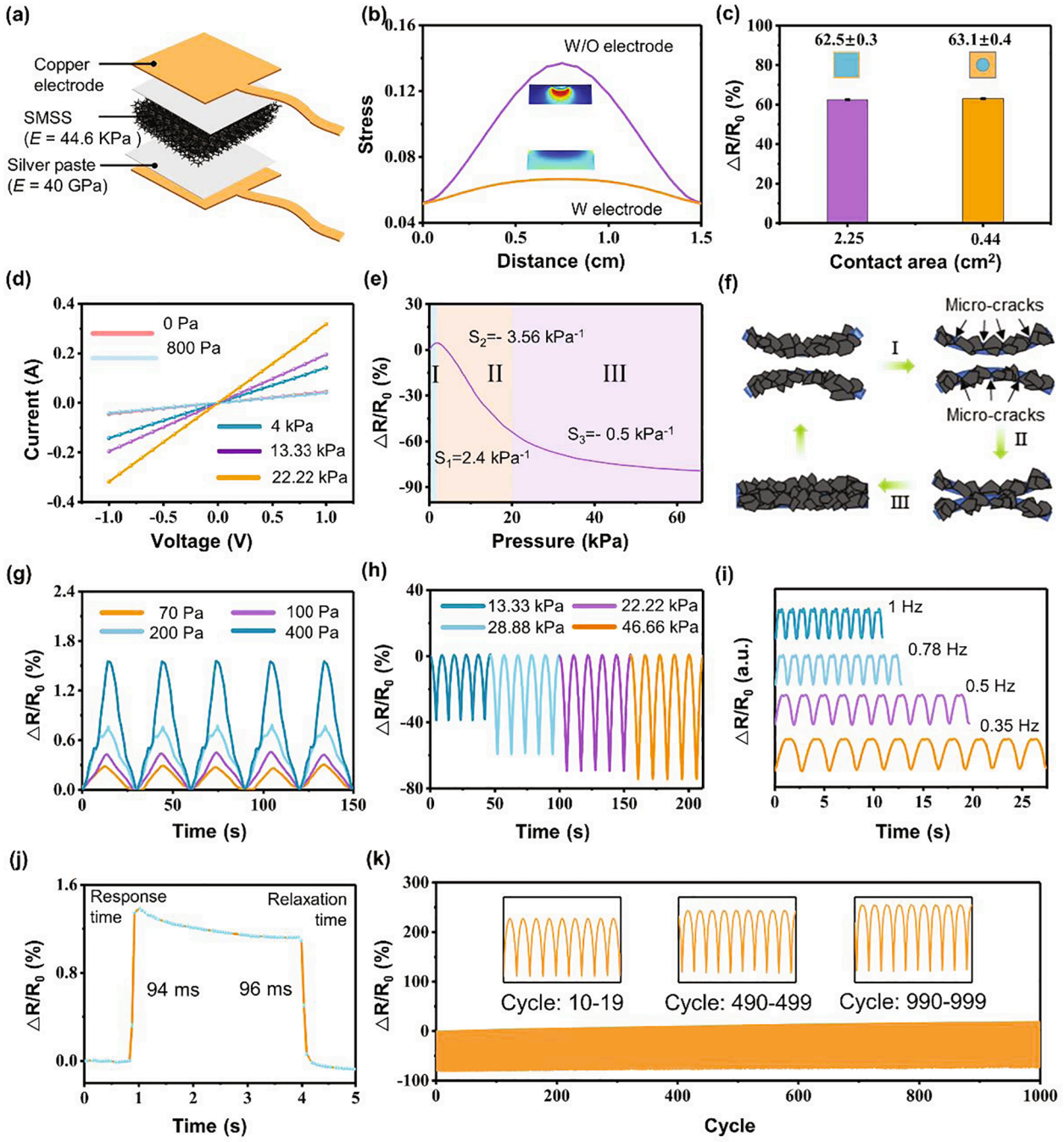

Fig. 3. Electromechanical properties of the SMSS pressure sensor. (a) Schematic illustration of the SMSS pressure sensor. (b) Stress distribution of the SMSS pressure sensor with and without electrode under external pressure with the Von-mises filed shown in the inset. (c) The relative resistance changes of the SMSS pressure sensor with different loading areas (2.25 and 0.44 cm^2). (d) I-V curves of the SMSS from −1 V to 1 V for an applied pressure of 0, 0.8, 4, 13.33, and 22.22 kPa. (e) Normalized relative resistance changes of the SMSS pressure sensor as a function of the applied pressure. (f) Schematic illustration of the evolution of the conductive pathway in the SMSS as the applied pressure increases. Dynamic response of the SMSS pressure sensor in five loading/unloading cycles for different pressure values in (g) region I and (h) region II, III in (e). (i) Dynamic response of the SMSS pressure sensor at different frequencies from 0.35 to 1 Hz. (j) Response and recovery times of the SMSS pressure sensor for a pressure of 400 Pa at a rate of 400 mm/min. (k) Durability test of the SMSS pressure sensor for 1000 cycles between 1 and 66 kPa at a rate of 200 mm/min.

be plotted as a function of the position of the advancing front of the air–liquid interface α (Fig. 2**g**). Because the critical bursting pressure ΔP_c corresponds to peak points, it is determined as 2.055 kPa for sweat and 2.145 kPa for water, which is the maximum pressure that the SMSS can sustain under external water impact. Therefore, the SMSS can sustain droplets or waterspout impact with splashing resistance in the dynamic wetting test, as shown in Fig. 2**h**.

2.3. Sensing performance of the SMSS pressure sensor

To evaluate the sensing performance of the SMSS, a series of electromechanical tests were carried out on the fabricated SMSS pressure sensor (Fig. 3**a**) with an applied voltage of 1 V unless otherwise specified. The mechanical performance of the SMSS and pristine sponges shown in **Fig. S11** indicates increased elastic modulus from 38.6 kPa of the pristine sponge to 44.6 kPa of the SMSS sponge due to the additional MXene-SA coatings. Moreover, the SMSS can be elastically compressed up to 42 kPa at 75% strain without plastic deformation, which is sufficient to detect most human motions [50]. Interestingly, the cured silver paste between the SMSS and copper electrodes transforms the localized pressure force into a more uniform pressure (Fig. 3**b**). Therefore, the SMSS with different loaded areas shows a similar resistance response (62.5 ± 0.3 % for 2.25 cm^2 vs. 63.1 ± 0.4 % for 0.44 cm^2 under 6 N loading) (Fig. 3**c**). The resulting SMSS pressure sensor can clearly detect the impact of ball drop (**Fig. S12 a),** with repeatable response as the ball drops from the same height (4 cm) (**Fig. S12 b**) and increased response as the height increases (from 3 cm to 5 cm, **Fig. S12 c**). The linear dependence of voltage from − 1 to 1 V on the current at different pressures in the I − V curves of the SMSS indicates a good ohmic contact between the SMSS pressure sensor and the copper electrode (Fig. 3**d**). The normalized relative resistance variation ($\Delta R/R_0$ with R_0 as the initial resistance) versus the applied pressure characterizes the sensing performance of the SMSS pressure sensor. For the SMSS pressure sensor with 0.5 mg/ml SA in Fig. 3**e**, three regions with different sensitivities ($S = \delta(\Delta R/R_0)/\delta P$) are observed: positive 2.4 kPa^{-1} in region I (0 – 1.85 kPa), negative 3.56 kPa^{-1} in region II (1.85 – 20 kPa), and negative 0.5 kPa^{-1} in region III (20 – 66.6 kPa). In region I, the deformation of the porous framework upon the applied pressure leads to the generation and propagation of the cracks, resulting in increased resistance (Fig. 3**f-I**). However, the further increase in the applied pressure leads to a dramatically increased contact area in the framework, which causes a sharp increase in the conductive pathway and a decrease in the resistance in region II (Fig. 3**f-II**). Following the saturation in the conductive pathway, region III shows a much smaller decrease in the resistance (Fig. 3**f-III**). The mechanism with the schematic shown in Fig. 3**c** is confirmed by the optical images (**Fig. S13**). The sensing performance comparison of the SMSS pressure sensor with different ratios of SA is also shown in **Fig. S14**. As the SA ratio increases from 0 to 0.5 and then to 1 mg/ml, the sensitivity of the SMSS pressure sensor decreases with the increasing SA ratio. The sensor with 0.5 mg/ml SA (i.e., the 50 mg SA/500 mg MXene) is chosen for the consideration of mechanical robustness and sensing performance in the subsequent studies unless specified otherwise. In the subsequent dynamic pressure testing, the SMSS first shows a highly repeatable response to repeated loading and unloading cycles for the pressure of 70, 100, 200, and 400 Pa at a rate of 200 mm/min in region I (Fig. 3**g**). A similar rapid and reliable response is observed for the applied pressure of 13.33, 22.22, 28.88, and 46.66 kPa in region II (Fig. 3**h**). The frequency-responsive curves of the SMSS pressure sensor show its capability to detect the frequency from 0.35 Hz to 1 Hz for an applied pressure of 1 kPa (Fig. 3**h**), which exceeds the rate range of normal human motions [51]. The rapid response is also confirmed by the fast response (94 ms) and recovery times (96 ms) for a pressure of 400 Pa at a rate of 400 mm/min (Fig. 3**j**). In addition, the pressure sensor exhibits excellent durability and stability in the dynamic cycling test for 1000 cycles (between 1 and 66 kPa and 0–1 kPa at 200 mm/min) (Fig. 3**k** and **Fig. S15**).

2.4. Electrothermal characterization of the SMSS pressure sensor

The SMSS with lower applied voltage and high heating efficiency can be ascribed to the increased conductive passways and higher conductivity (12 Ω and 0.055 S/cm at 10% RH, **Fig. S3 b**) [52–56]. For an applied voltage (U), the electrical power (P) generated by the sensors is given by Joule's law as $P = U^2/R$, where R is the resistance of the sensor. Since the 3D sponge results in non-uniform temperature distribution on the sample surface, the peak temperature is used to characterize the Joule heating effect in our work. Because the peak temperature rises in the SMSS scale linearly with the heating power (or the square of the supplied voltage, **Fig. S16**), the voltage exhibits a dramatic effect to modulate the temperature (Fig. 4**a**). As the applied voltage increases from 1 to 5 V, the peak temperature rises in the SMSS pressure sensor as captured by an infrared (IR) camera (Fig. 4**a**, inset) and a thermocouple increase from 28 to 122 °C. Notably, the lower applied voltage is also beneficial for safe operation with less energy consumption. The peak temperature (T_{max}) of 86.8 °C is also well maintained during 5 cyclic on − off heating cycles for an input voltage of 4 V (Fig. 4**b**), indicating outstanding repeatability and durability for long-term use. The long-term heating stability and reliability of the SMSS pressure sensor are confirmed by the quickly saturated and then steady temperature evolution with time over 9000 s at a constant voltage of 4 V (Fig. 4**c**). Although the high temperature may cause an adverse thermal effect on the skin, there is a large temperature difference between the SMSS sensor and electrode surface (Fig. 4**d**). While the peak temperature in the SMSS reaches 84.7 °C and 103.3 °C for a voltage of 4 V and 4.5 V, the electrode connected to the SMSS via a conductive silver paste exhibits a temperature of 48.4 °C and 55.6 °C, respectively (Fig. 4**e**). The temperature difference is likely attributed to the higher resistance of the SMSS compared to that of the electrode. [58] The high temperature generated at the surface of the SMSS can significantly accelerate the evaporation of water droplets, with a 10-fold increase in the evaporation rate compared to the one without heating (Fig. 4**f**). For the same applied voltage, the Joule heating-induced temperature rise also changes with the applied pressure due to the varied resistance (Fig. 4**g**). As a result, the peak temperature rise first slightly decreases and then increases with the increasing pressure. The increase in the temperature with a small variation in the range (e.g., 100.8 °C − 102 °C at 4 V) yields a stable sensing performance during the dynamic compression process (0.45 Hz) (Fig. 4**h**).

2.5. Humidity-insensitivity of the SMSS pressure sensor from Joule heating

The small size water vapor can nucleate and grow on the superhydrophobic surface to cause degraded superhydrophobicity. To address this challenge, the Joule heating with an accelerated evaporation rate is further exploited to reduce adsorption of water molecules for sustained superhydrophobicity. Compared with the almost unchanged resistance of the sensor in the 10% RH condition, the sensor placed in the 70% RH condition shows a decreased resistance as heating drives out the adsorbed water molecules (**Fig. S17**). The static resistance changes of the SMSS with or without heating (4 V) in 70% RH or saturated water vapor conditions are also compared. In the 70% RH, the SMSS pressure sensor shows an 8.6-fold reduction in resistance increase compared to the one without heating (11 % versus 95 %, Fig. 5**a light line**). Meanwhile, the resistance increase of the SMSS with heating is also 11.7 times smaller than the one without heating (21% versus 250.9 %, Fig. 5**a dark line**) in the saturated water vapor condition. The performance enhancement from the heating is even more significant in both high humidity and saturated water vapor environment, as the SMSS pressure sensor is cycled. The SMSS pressure sensor without heating shows a large increase of 40.4 % in the resistance response in the 70% RH (Fig. 5**b**), which is still smaller than that of 56% from the MXene-SA pressure sensor without Hf-SiO_2 coating (**Figure S18**). Meanwhile, the

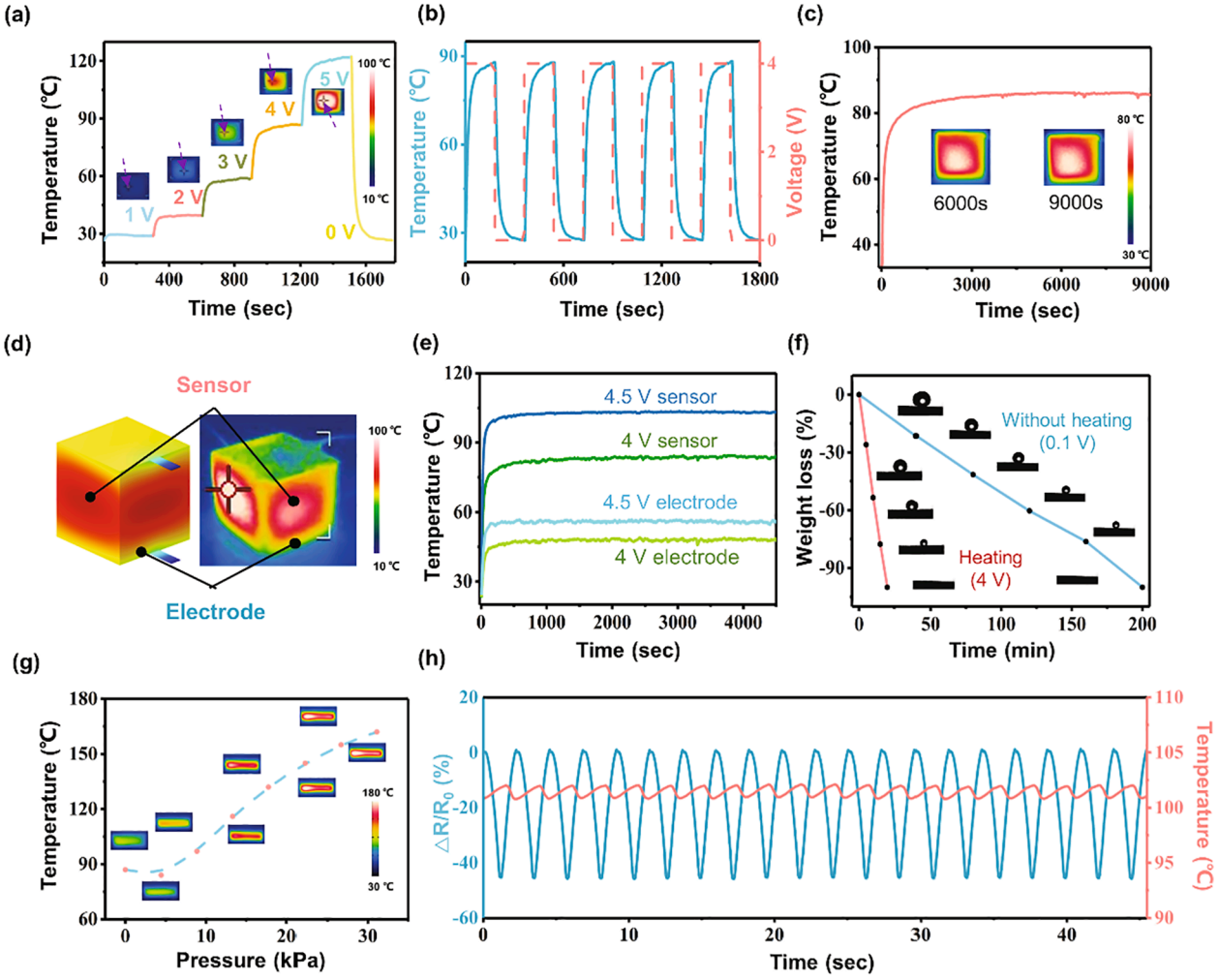

Fig. 4. Electrothermal performance of the SMSS pressure sensor. (a) The time-dependent peak temperature of the SMSS sponge for stepwise increased voltage from 1 to 5 V, with the IR images shown in the insets (peak temperature indicated by cross marks). (b) Thermal cycling for five on–off cycles and (c) temperature stability for an applied voltage of 4 V. (d) The finite element simulation (left) and experimental (right) results illustrate the difference between the peak temperature in the sensor and value at the electrode surface, along with (e) their time-dependent evolution measured in the experiment for a voltage of 4 V and 4.5 V. (f) The volume evolution of a water droplet (15 μL) on the SMSS pressure with (red, 4 V) and without (blue, 0.1 V) heating. (g) The pressure-dependent peak temperature of the SMSS sponge (4 V) for stepwise increased pressure up to 31.11 kPa, with the IR images shown in the insets. (h) The dynamic temperature and response changes of the SMSS pressure sensor (4 V) under a 15.55 kPa cycling pressure.

SMSS pressure sensor with heating only exhibits a small resistance change of ca. 4.3 % (Fig. 5**c**), which is a 9.4-fold enhancement over the one without heating. In saturated water vapor conditions, the dynamic resistance response of the SMSS pressure sensor with heating also shows a 23.7-fold enhancement compared to the one without heating (8.96 % versus 212.37 %, **Fig. S19**). The humidity-insensitive mechanism is further explained by studying the thickness change in the MXene-SA coating (Fig. 5**d**). Without heating, the water molecules in the high humidity environment trapped inside the interspaces between MXene nanosheets expand the MXene interlayer (or sheet-to-sheet) distance to increase the tunneling resistance. In the water vapor case, the large number of water molecules further increases the MXene interlayer distance to result in an increased resistance (Fig. 5**e, top**). In comparison, the SMSS with heating prevents the adsorption of water molecules to maintain a relatively stable MXene interlayer distance (Fig. 5**e, bottom**). In particular, the film thickness increases by 3% (or 5.2%) in the 90% RH (or saturated water vapor) environment with heating, which is much smaller than 14.5% (or 45.6%) in the samples without heating (Fig. 5**f**).

The water molecule condensation within the superhydrophobic surface can also cause the degradation of superhydrophobicity in high humidity or saturated water vapor conditions. For example, the superhydrophobic surface on the glass substrate in the saturated water vapor condition shows obvious degradation from superhydrophobicity to hydrophilicity with CA reduced from 156° to 55° (**Fig. S20 a**). The process of surface wettability transformation can be explained by a 2D free energy thermodynamic model (**Fig. S21**) [57,58]. The thermodynamic status of the non-wetting system (Cassie's state) and humidity-induced wetting system (Wenzel's state) is related to the surface geometrical configurations of the system. The normalized change of free energy (FE) per unit length of contact line for a water droplet moving from a reference position (size of L_0 and apparent contact angle of θ_0) to an arbitrary position with L_{ar} and θ_{ar} can be written as (see Methods in Supporting Information)

$$\Delta F_{0\to ar} = \left(\theta_{ar}\frac{L_{ar}}{sin\theta_{ar}} - \theta_0\frac{L_0}{sin\theta_0}\right) \pm \Theta(L_{ar}) \quad (1)$$

The last term $\Theta(L_{ar})$ in Eq. (1) represents the change of the FE at solid–liquid and solid-air interface beneath the droplet, with the positive (or negative) sign corresponding to receding (or advancing) of the water droplet. The constant droplet volume between two states gives

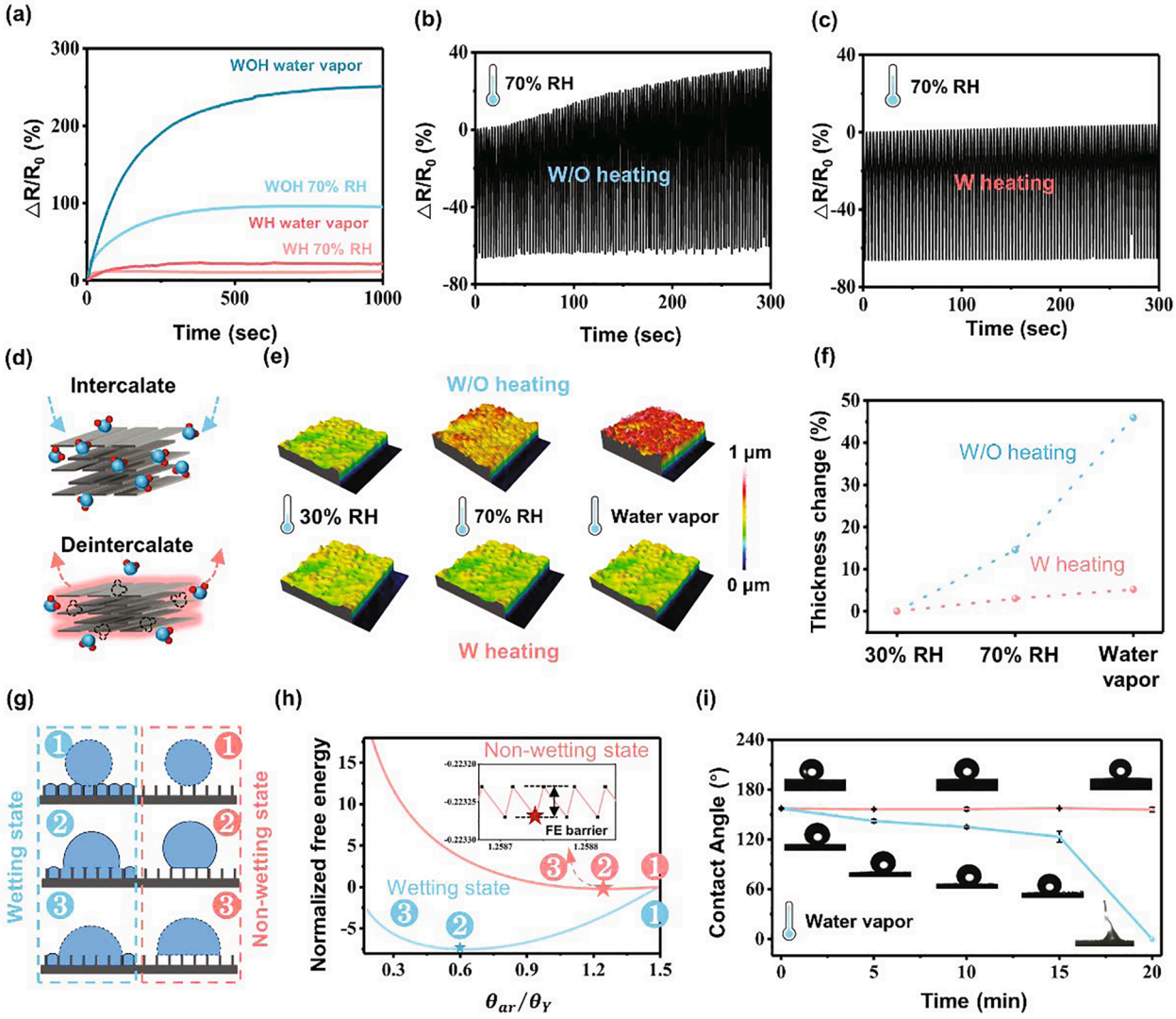

Fig. 5. Sustained superhydrophobicity of the SMSS from Joule heating in the moisture environment. (a) The normalized relative resistance change of the SMSS with (red) and without heating (blue) in both 70% RH and water vapor environments. The normalized relative resistance change for a dynamic pressure loading of 28.88 kPa was applied on the SMSS (b) without and (c) with heating that is cycled in the 70% RH. (d) Schematic illustrations showing the water molecule intercalation into MXene-SA (top) and the effect of Joule heating (bottom). (e) 3D optical images of the thickness change in the MXene-SA film without (top) or with (bottom) Joule heating in the dry, humid, and saturated water vapor environment. (f) The measured thickness change in the MXene-SA film with (red) or without (blue) Joule heating from (e). (g) Schematic illustrations to show the wetting and non-wetting states of the surface with a representative microstructure. (h) The normalized FE as a function of CA for the non-wetting and wetting systems with 1/2/3 corresponding to the initial/stable/metastable states (surface profile: $b = h = 3a$, $L_0 = 1000a$, $\theta_0 = 179^0$ and $\theta_Y = 120^0$). The inset shows the FE barrier. (i) Changes in the contact angle on the SMSS pressure sensor with the exposure time in the saturated water vapor environment (red or blue: with or without heating).

$$\theta_{ar}\left(\frac{L_{ar}}{sin\theta_{ar}}\right)^2 - L_{ar}^2 ctg\theta_{ar} = \theta_0\left(\frac{L_0}{sin\theta_0}\right)^2 - L_0^2 ctg\theta_0 + \Psi(L_{ar}) \quad (2)$$

The last term in Eq. (1) and Eq. (2) for wetting and non-wetting systems are presented in **Methods (Supporting Information)**. In a representative system with a given surface profile ($b = h = 3a$, $L_0 = 1000a$, $\theta_0 = 179^0$, and intrinsic CA of $\theta_Y = 120^0$), the FE variation can be obtained from Eqs. (1–2) as a function of the apparent CA (θ_{ar}), with 3 selected points to highlight the initial, stable, and metastable states (Fig. 5**g**). The lowest point on the FE curve corresponds to the stable state with an apparent contact angle of θ_e and the local variation between valleys and peaks indicates the maximum FE barrier (Fig. 5**h, inset**). In Fig. 5**h**, the FE curve of the wetting system is located below that of a non-wetting one and the apparent CA (θ_e) at the stable state in the wetting system ($\theta_e^{wetting} < \theta_Y$) is much smaller than that of the non-wetting system ($\theta_e^{non-wetting} > \theta_Y$). As a result, the humidity-induced water molecules in the troughs of the microstructures could transition the system from the non-wetting to a more stable wetting state. As the condensation of water molecules would degrade the superhydrophobicity, the effectively reduced condensation of water molecules from heating (100 °C) exhibits sustained superhydrophobicity for more than 60 min in a saturated water vapor environment (Fig. S20 **b**). For the SMSS pressure sensor (4 V), the Joule heating effect is important to prevent condensation of water molecules and maintain the superhydrophobicity even in a saturated water vapor environment for 20 min (Fig. 5**i, red line**). In comparison, the sensor without Joule heating shows a continuously decreased superhydrophobicity with the increasing exposure time, which further results in penetration into the porous pressure sensor (Fig. 5**i, blue line**).

2.6. Applications of the moisture-insensitive SMSS pressure sensor

The SMSS pressure sensor with high sensitivity, large sensing range,

and sustained superhydrophobicity under high humidity or saturated water vapor environments compares favorably over the other superhydrophobic pressure sensors reported in the literature (**Fig. S22** and Table 1) [13,32–34,36,43,53,59,60]. Moreover, the self-adhesive rubber is spin-coated onto the electrode surface to provide improved skin-device adhesion and further enhanced thermal isolation in this work (Fig. 6**a**). The resulting self-adhesive SMSS pressure sensor can be directly mounted onto diverse substrates, including glass, textile, paper, and human skin (Fig. 6**b**). Meanwhile, the low thermal conductivity of self-adhesive rubber further isolates the heating and prevents the adverse thermal effect on the skin, with the temperature reduced from 109 °C on the SMSS to 40 °C at the rubber/skin interface (Fig. 6**c**). Hence, conveniently attached to the skin of different human body locations, the SMSS pressure sensors can provide moisture-insensitive detection of various human motions in a complex all-weather environment. Firstly, the subtle pressure from pulsation can be detected by the SMSS pressure sensor on a human wrist in real-time over 4.8 s with a frequency of 62 beats min^{-1} (Fig. 6**d**). Ascribed to the adhesive layer, the devices that are tightly attached to the skin can detect human pulse more precisely (Fig. 6**d inset**) compared to the one without adhesive layer (**Fig. S23**). The large deformation such as elbow bending at different degrees (i.e., 0°, 30°, 90°, and 130°) can also be easily captured by the SMSS pressure sensor on the human elbow (**Fig. S24**). In particular, the motion detections such as repeated wrist bending (Fig. 6**e**) or hand squeezing (Fig. 6**f**) are not affected by intermittent water droplets (to simulate the rainy conditions) due to the immediate rolling off of the droplets on the superhydrophobic surface. More impressively, the SMSS pressure sensor is mounted onto the human knee to detect the motions of knee bending and relaxing under dry (30% RH) and wet (70% RH) conditions (Fig. 6**g**). The SMSS pressure sensor with heating shows a similar resistance response between dry and wet conditions. The SMSS pressure sensor on the index finger with heating can also robustly detect the finger bending in water vapor environments (Fig. 6**h, top panel**). The SMSS sensor with heating exhibits a much more stable signal (Fig. 6**h, bottom panel**), demonstrating the effectiveness of Joule heating in a water vapor environment (e.g., fog).

3. Conclusion

In summary, this work reports the SMSS pressure sensor with Joule heating to provide sustained superhydrophobicity and moisture-resistant sensing. The sustained superhydrophobicity comes from the efficient low-voltage Joule heating contributed by the highly conductive MXene-SA coating, which reduces adsorption of water molecules during both the static and dynamic pressure cycling. The special electrode design minimizes the adverse thermal effect on the skin and provides a more uniform pressure loading to reduce the response error caused by the varied contact areas. Therefore, the resulting moisture-insensitive SMSS pressure sensor with high sensitivity, large sensing range, excellent flexibility, and sustained superhydrophobicity demonstrates high potential to detect various human motions in all-weather conditions especially the high humidity or water vapor environments. The design and demonstration of our SMSS pressure sensor could also provide the other biophysical and biochemical sensors with sustained superhydrophobicity and reliable sensing performance toward the next-generation stretchable epidermal electronics.

4. Materials and Methods

4.1. Materials

A commercial melamine–formaldehyde sponge (Shanghai Beiyou Buiding Material Co., Led.) was selected as the substrate. Layered ternary carbide (Ti_3AlC_2) MAX phase powder and polypropylene membrane were procured from 11 Technology Co., Ltd. Concentrated hydrochloric acid (HCl, technical grade, 35%-38%) was provided by Hunan Huihong Reagent Co., Ltd. Sodium alginate (SA), lithium fluoride (LiF, 99.9%), and ethanol were purchased from Aladdin Biochemical Technology Co., Ltd. Hydrophobic fumed silica nanoparticles R202 were obtained from Evonik Industries Co. Ltd., Germany. Self-adhesive silicon rubber (9500 A/B) was purchased from Hongyejie Technology Co., Ltd.

4.2. Synthesis of $Ti_3C_2T_x$ MXene nanosheets and MXene-SA dispersion

MXene ($Ti_3C_2T_x$) was synthesized by selectively etching the Ti_3AlC_2 MAX phase with LiF/HCl solution. In the typical process, LiF of 3.2 g was slowly dissolved in 9 M HCl of 40 mL in a Teflon container under magnetic stirring for ca. 1 h to ensure complete dissolution of LiF. Next, Ti_3AlC_2 powder of 2 g was slowly added into the LiF/HCl etching solution (within 5 min), and the mixture was allowed to react at 35 °C under magnetic stirring for 24 h, yielding a stable suspension. The resultant $Ti_3C_2T_x$ suspension was repeatedly washed with deionized water and centrifuged at 3500 rpm for 5 min until the supernatant showed dark green with pH greater than 5. The swollen black $Ti_3C_2T_x$ slurry was redissolved by adding deionized water of 40 mL into the whole sediment. After centrifugation at 3500 rpm for 2 min, the dark concentrated supernatant of $Ti_3C_2T_x$ nanosheets was collected. The further delamination of $Ti_3C_2T_x$ was conducted by sonication followed by centrifugation at 3500 rpm for 1 h, yielding homogeneous supernatant with delaminated $Ti_3C_2T_x$ nanosheets. The concentration of the resultant MXene colloidal solution was determined by filtering a known volume of the solution through a polypropylene filter (Celgard 3501 coated PP) and measuring the weight of the resulting freestanding film after vacuum drying. Further dilution of the resultant MXene colloidal solution resulted in the 5 mg mL^{-1} MXene solution. Next, 50 mg SA was added into the 100 mL MXene solution and stirred for 30 min, leading to the SA concentration of 0.5 mg mL^{-1} in the mixed MXene solution.

Table 1
Comparison of the overall performance of present SMSS pressure sensor with previously reported pressure sensors.

Hydrophobic materials	Pressuresensitivity	Sensingrange	Joule heating	Waterinsensitivity	Humidity insensitivity	Water molecules condensation	Ref
CNT	0.515 kPa^{-1}	3 kPa	–	hydrophobic	No	Yes	[59]
FAS-modified rGO	4.97 kPa^{-1}	3 kPa	–	154°	–	Yes	[13]
Ag NPs	0.013 kPa^{-1}	80 kPa	0.8 V/70 °C	151°	–	–	[34]
Hf-SiO_2	0.39 kPa^{-1}	5 kPa	–	145°	–	Yes	[53]
PDMS@MXene	5.78 kPa^{-1}	20 kPa	4 V/118.7 °C	135.6°	–	–	[43]
FAS-modified MXene	3.84 kPa^{-1}	12.4 kPa	–	157°	–	Yes	[60]
ODI-modified TiO_2	0.83 kPa^{-1}	45 kPa	–	141.8°	S	Yes	[33]
CNT	1.14 kPa^{-1}	600 kPa	–	155°	S	Yes	[32]
N-dodecanethiol-modified	0.144 kPa^{-1}	2.72 kPa	–	153.1°	S/D	Yes	[36]
Hf-SiO_2	3.56 kPa^{-1}	66.6 kPa	5 V/122 °C	158.2°	S/D	No	※

FAS: 1H,1H,2H,2H-perfluorooctyltriethoxysilane; ODI: octadecyl isocyanate;

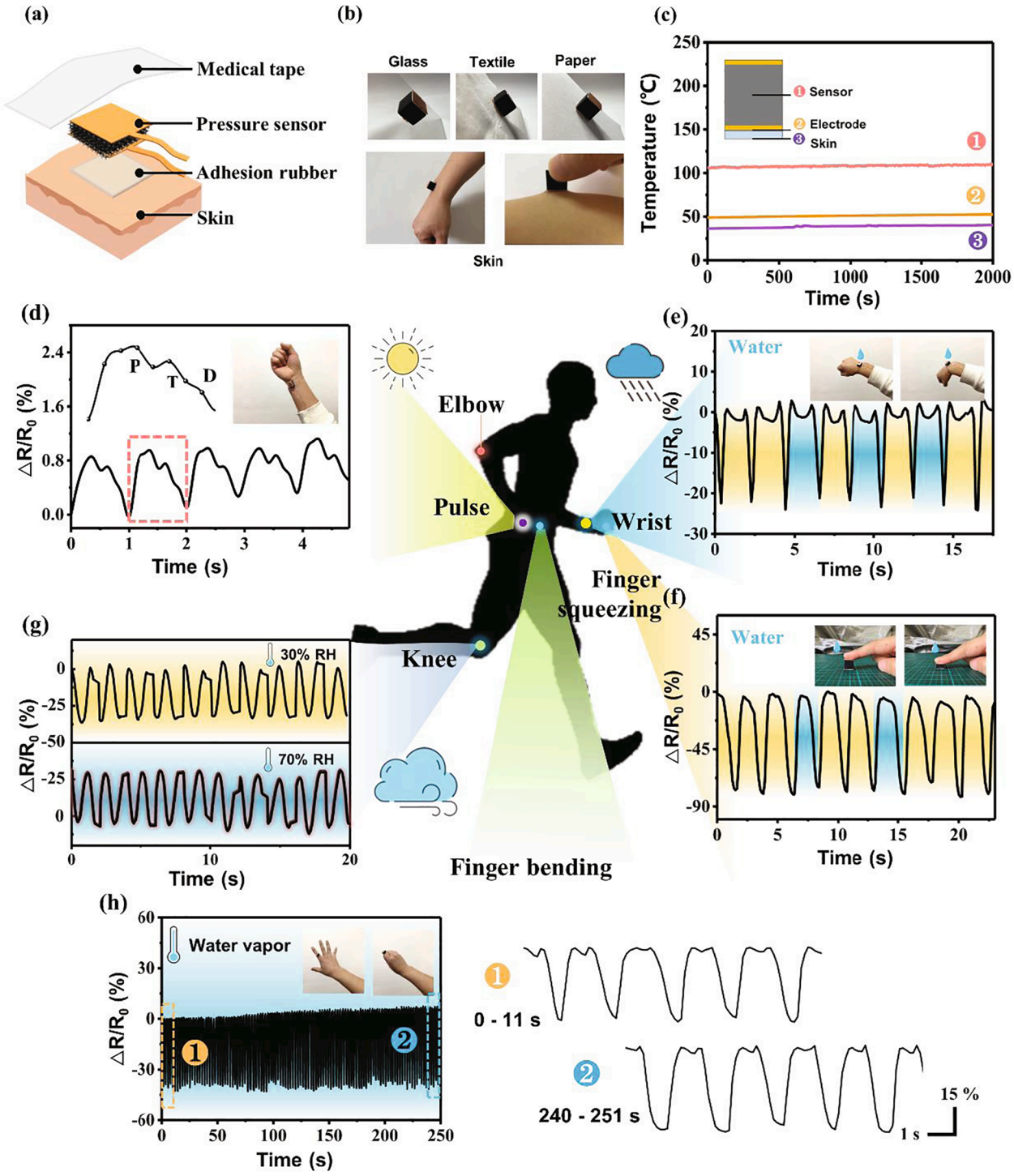

Fig. 6. The demonstration of the self-adhesive moisture-insensitive SMSS from Joule heating to detect various human motions. (a) Schematic illustration of the self-adhesive moisture-insensitive SMSS mounted onto the human skin for real-time detection of human motions. (b) Photographs of the self-adhesive SMSS pressure sensor on diverse substrates. (c) Temperature evolution in varying locations of the SMSS pressure sensor (4.5 V). (d) Pulse signal detected by the SMSS pressure sensor on the wrist (magnified images of a signal pulse and a photograph shown in the inset). The motions of repeated (e) wrist bending and (f) hand squeezing captured by the SMSS pressure sensor, which shows robustness performance even in the presence of intermittent water droplets. (g) The resistance response of the SMSS pressure sensor with heating on the knee joint to detect its motions under wet (70% RH) and dry (30% RH) environments. (h) The SMSS pressure sensor with the heating on the finger joint to detect extending and clenching of the hand in the water vapor environment, with the magnified initial (h1) and final (h2) resistance responses shown in right panels.

4.3. Preparation of SMSS pressure sensors.

After the commercial MF sponge (Shanghai Beiyou Buiding Material Co., Ltd.) as the substrate was cut into 1.5 × 1.5 × 1.5 cm^3 cubes, they were alternatively cleaned by acetone and distilled water twice in an ultrasonic cleaner. The resulting sponge cubes were dried in a vacuum oven at 100 °C for 5 h to completely remove moisture. Next, these precleaned sponge cubes dipped in the dispersion (MXene of 5 mg mL^{-1}

and SA of 0.5 mg mL^{-1}) further underwent vacuum degassing at 100 °C for 12 h or centrifugation at 1000 rpm for 1 min to ensure uniform coating. Multiple layers of MXene-SA composites were coated by repeating the "dipping and drying" process. Spray coating of the commercial hydrophobic silica (Hf-SiO_2) nanoparticles in PDMS and ethanol mixed solution (3 wt% Hf-SiO_2, 0.1 wt% PDMS) on MXene-SA sponges, followed by vacuum degassing at 100 °C for 2 h, achieved further hydrophobic modification to yield SMSS cubes. Connecting two wires-welded electrodes to the top and bottom sides of SMSS cubes via conductive silver paste allowed the signal measurements with a digital multimeter. Self-adhesive materials are spin-coated onto the bared regions of the electrode surface to improve the stickiness. The different voltages were applied by a direct-current (DC) power supply (2280S, Keithly Instruments, Inc., Cleveland, OH).

4.4. Characterizations.

The sample morphology was analyzed by a field emission scanning electron microscope (SU5000, Hitachi, Japan) at an accelerating voltage of 25 kV. Energy-dispersive X-ray spectroscopy (EDX) and mapping were also acquired with the same equipment. X-ray diffraction (XRD) curves were recorded on an X'Pert PRO XRD using Cu-Kα radiation and a scanning speed of 5°/min. X-ray photoelectron spectroscopy (XPS) was obtained using a Thermo Scientific K-Alpha instrument. Fourier transform infrared (FTIR) spectra were obtained using a Thermo Nicolet NEXUS-6700 FTIR instrument in the attenuated total reflection mode. Mercury intrusion porosimetry was obtained using a MicroActive AutoPore V9620. The contact angles of the samples were measured using a Model 250 (p/n 250-F1) optical contact-angle goniometer (Rame-hart, USA) at ambient temperature. The average CA was obtained by measurements from more than five different positions on the same sample. The mechanical properties were measured using a universal testing machine (ZQ-990A-1). The electrical characteristics of the strain sensor were measured using a digital source meter (2400, Keithly Instruments, Inc., Cleveland, OH). Humidity and water vapor response performances were conducted using a homemade humid air and water vapor generator. The IR images and the surface temperature distributions of the heating device were recorded using an IR thermal camera (FLIR, E4).

Declaration of Competing Interest

The authors declare that they have no known competing financial interests or personal relationships that could have appeared to influence the work reported in this paper.

Acknowledgement

This research was supported by the National Natural Science Foundation of China (12172319, 11872326 and 12002295), Natural Science Foundation of Hunan Province (2021JJ30648 and 2021JJ30641), Scientific Research Fund (2018-356) of Hunan Provincial Education Department, Postgraduate Scientific Research Innovation Project of Hunan Province (CX20200629). H. C. also acknowledges the support from the National Science Foundation (NSF) (Grant No. ECCS-1933072), the National Institutes of Health (Award Nos. R61HL154215 and R21EB030140), and Penn State University.

Appendix A. Supplementary data

Supplementary data to this article can be found online at https://doi.org/10.1016/j.cej.2021.134370.

References

[1] S. Pyo, J. Lee, K. Bae, S. Sim, J. Kim, Recent progress in flexible tactile sensors for human-interactive systems: from sensors to advanced applications, Adv. Mater. 33 (47) (2021) 2005902, https://doi.org/10.1002/adma.v33.4710.1002/adma.202005902.
[2] Z. Lou, L. Wang, K. Jiang, Z. Wei, G. Shen, Reviews of wearable healthcare systems: Materials, devices and system integration, Mater. Sci. Eng. R. 140 (2020) 100523, https://doi.org/10.1016/j.mser.2019.100523.
[3] Y. Liu, R. Bao, J. Tao, J. Li, M. Dong, C. Pan, Recent progress in tactile sensors and their applications in intelligent systems, Sci. Bull. 65 (1) (2020) 70–88.
[4] Y. Song, H. Chen, Z. Su, X. Chen, L. Miao, J. Zhang, X. Cheng, H. Zhang, Highly compressible integrated supercapacitor-piezoresistance-sensor system with CNT-PDMS sponge for health monitoring, Small 13 (2017) 1702091.
[5] S. Zhao, R. Zhu, High sensitivity and broad range flexible pressure sensor using multilayered porous PDMS/AgNP sponge, Adv. Mater. Technol. 4 (2019) 1900414.
[6] Y. Cheng, Y. Ma, L. Li, M. Zhu, Y. Yue, W. Liu, L. Wang, S. Jia, C. Li, T. Qi, J. Wang, Y. Gao, Bioinspired microspines for a high-performance spray Ti3C2Tx MXene-based piezoresistive sensor, ACS Nano 14 (2) (2020) 2145–2155.
[7] Y. Xiao, Y.u. Duan, N. Li, L. Wu, B.o. Meng, F. Tan, Y. Lou, H. Wang, W. Zhang, Z. Peng, Multilayer double-sided microstructured flexible iontronic pressure sensor with a record-wide linear working range, ACS Sens. 6 (5) (2021) 1785–1795, https://doi.org/10.1021/acssensors.0c0254710.1021/acssensors.0c02547.s001.
[8] K. Wang, Z. Lou, L. Wang, L. Zhao, S. Zhao, D. Wang, W. Han, K. Jiang, G. Shen, Bioinspired interlocked structure-induced high deformability for two- dimensional titanium carbide (MXene)/natural microcapsule-based flexible pressure sensors, ACS Nano 13 (8) (2019) 9139–9147.
[9] Y. Qiu, Y. Tian, S. Sun, J. Hu, Y. Wang, Z. Zhang, A. Liu, H. Cheng, W. Gao, W. Zhang, H. Chai, H. Wu, Bioinspired, multifunctional dual-mode pressure sensors as electronic skin for decoding complex loading processes and human motions, Nano Energy 78 (2020), 105337.
[10] L.-Q. Tao, K.-N. Zhang, H.e. Tian, Y. Liu, D.-Y. Wang, Y.-Q. Chen, Y.i. Yang, T.-L. Ren, Graphene- paper pressure sensor for detecting human motions, ACS Nano 11 (9) (2017) 8790–8795.
[11] W. Chen, L.-X. Liu, H.-B. Zhang, Z.-Z. Yu, Kirigami-inspired highly stretchable, conductive, and hierarchical $Ti_3C_2T_x$ MXene films for efficient electromagnetic interference shielding and pressure sensing, ACS Nano 15 (4) (2021) 7668–7681, https://doi.org/10.1021/acsnano.1c0127710.1021/acsnano.1c01277.s001.
[12] D. Wang, L. Wang, Z. Lou, Y. Zheng, K. Wang, L. Zhao, W. Han, K. Jiang, G. Shen, Biomimetic, biocompatible and robust silk Fibroin-MXene film with stable 3D cross-link structure for flexible pressure sensors, Nano Energy 78 (2020), 105252.
[13] J. Wu, H. Li, X. Lai, Z. Chen, X. Zeng, Conductive and superhydrophobic F- rGO@CNTs/chitosan aerogel for piezoresistive pressure sensor, Chem. Eng. J. 386 (2020), 123998.
[14] Y. Jeong, J. Park, J. Lee, K. Kim, I. Park, Ultrathin, biocompatible, and flexible pressure sensor with a wide pressure range and its biomedical application, ACS Sens. 5 (2) (2020) 481–489.
[15] X. Li, Y.J. Fan, H.Y. Li, J.W. Cao, Y.C. Xiao, Y. Wang, F. Liang, H.L. Wang, Y. Jiang, Z.L. Wang, G. Zhu, Ultracomfortable hierarchical nanonetwork for highly sensitive pressure sensor, ACS Nano 14 (8) (2020) 9605–9612.
[16] H. Liu, H. Xiang, Y. Wang, Z. Li, L. Qian, P. Li, Y. Ma, H. Zhou, W. Huang, A flexible multimodal sensor that detects strain, humidity, temperature, and pressure with carbon black and reduced graphene oxide hierarchical composite on paper, ACS Appl. Mater. Interfaces 11 (43) (2019) 40613–40619.
[17] C. Ma, D. Xu, Y.-C. Huang, P. Wang, J. Huang, J. Zhou, W. Liu, S.-T. Li, Y.u. Huang, X. Duan, Robust flexible pressure sensors made from conductive micropyramids for manipulation tasks, ACS Nano 14 (10) (2020) 12866–12876.
[18] Y. Pei, X. Zhang, Z. Hui, J. Zhou, X. Huang, G. Sun, W. Huang, $Ti_3C_2T_X$ MXene for Sensing Applications: Recent Progress, Design Principles, and Future Perspectives, ACS Nano 15 (2021) 3996–4017.
[19] M. Xin, J. Li, Z. Ma, L. Pan, Y. Shi, MXenes and Their Applications in Wearable Sensors, Front Chem 8 (2020) 297.
[20] S.-N. Li, Z.-R. Yu, B.-F. Guo, K.-Y. Guo, Y. Li, L.-X. Gong, L.i. Zhao, J. Bae, L.-C. Tang, Environmentally stable, mechanically flexible, self-adhesive, and electrically conductive Ti3C2TX MXene hydrogels for wide-temperature strain sensing, Nano Energy 90 (2021) 106502, https://doi.org/10.1016/j.nanoen.2021.106502.
[21] M. Mao, K.-X. Yu, C.-F. Cao, L.-X. Gong, G.-D. Zhang, L.i. Zhao, P. Song, J.-F. Gao, L.-C. Tang, Facile and green fabrication of flame-retardant Ti3C2Tx MXene networks for ultrafast, reusable and weather-resistant fire warning, Chemical Engineering Journal 427 (2022) 131615, https://doi.org/10.1016/j.cej.2021.131615.
[22] H. An, T. Habib, S. Shah, H. Gao, A. Patel, I. Echols, X. Zhao, M. Radovic, J. Green, L. Lutkenhaus, Water Sorption in MXene/Polyelectrolyte Multilayers for Ultrafast Humidity Sensing, ACS Applied Nano Materials 2 (2019) 948–955.
[23] X. Zhao, L.-Y. Wang, C.-Y. Tang, X.-J. Zha, Y. Liu, B.-H. Su, K. Ke, R.-Y. Bao, M.-B. Yang, W. Yang, Smart $Ti_3C_2T_x$ MXene fabric with fast humidity response and Joule heating for healthcare and medical therapy applications, ACS Nano 14 (7) (2020) 8793–8805.
[24] Y. Zhang, Y. Chen, J. Huang, Y. Liu, J. Peng, S. Chen, K. Song, X. Ouyang, H. Cheng, X. Wang, Skin-interfaced microfluidic devices with one-opening chambers and hydrophobic valves for sweat collection and analysis, Lab Chip 20 (15) (2020) 2635–2645.
[25] Y. Bu, T. Shen, W. Yang, S. Yang, Y. Zhao, H. Liu, Y. Zheng, C. Liu, C. Shen, Ultrasensitive strain sensor based on superhydrophobic microcracked conductive

$Ti_3C_2T_x$ MXene/paper for human-motion monitoring and E-skin, Sci. Bull. (2021), https://doi.org/10.1016/j.scib.2021.04.041.
[26] L. Li, Y. Bai, L. Li, S. Wang, T. Zhang, A superhydrophobic smart coating for flexible and wearable sensing electronics, Adv. Mater. 29 (2017) 1702517.
[27] H. Liu, Q. Li, Y. Bu, N. Zhang, C. Wang, C. Pan, L. Mi, Z. Guo, C. Liu, C. Shen, Stretchable conductive nonwoven fabrics with self-cleaning capability for tunable wearable strain sensor, Nano Energy 66 (2019), 104143.
[28] Q. Li, H. Liu, S. Zhang, D. Zhang, X. Liu, Y. He, L. Mi, J. Zhang, C. Liu, C. Shen, Z. Guo, Superhydrophobic Electrically Conductive Paper for Ultrasensitive Strain Sensor with Excellent Anticorrosion and Self-Cleaning Property, ACS Appl. Mater. Interfaces 11 (2019) 21904–21914.
[29] S. Wang, X. Du, Y. Luo, S. Lin, M. Zhou, Z. Du, X. Cheng, H. Wang, Hierarchical design of waterproof, highly sensitive, and wearable sensing electronics based on MXene-reinforced durable cotton fabrics, Chemical Engineering Journal 408 (2020), 127363.
[30] J. Lin, X. Cai, Z. Liu, N. Liu, M. Xie, B. Zhou, H. Wang, Z. Guo, Anti-liquid-Interfering and Bacterially Antiadhesive Strategy for Highly Stretchable and Ultrasensitive Strain Sensors Based on Cassie-Baxter Wetting State, Adv. Funct. Mater. 30 (2020) 2000398.
[31] F. Wang, J. Jiang, F. Sun, L. Sun, T. Wang, Y. Liu, M. Li, Flexible wearable graphene/alginate composite non-woven fabric temperature sensor with high sensitivity and anti-interference, Cellulose 27 (4) (2020) 2369–2380.
[32] L. Wang, X. Huang, D. Wang, W. Zhang, S. Gao, J. Luo, Z. Guo, H. Xue, J. Gao, Lotus leaf inspired superhydrophobic rubber composites for temperature stable piezoresistive sensors with ultrahigh compressibility and linear working range, Chemical Engineering Journal 405 (2021) 127025, https://doi.org/10.1016/j.cej.2020.127025.
[33] L. Yang, J. Ma, W. Zhong, Q. Liu, M. Li, W. Wang, Y. Wu, Y. Wang, X. Liu, D. Wang, Highly accurate fabric piezoresistive sensor with anti-interference of both high humidity and sweat based on hydrophobic non-fluoride titanium dioxide nanoparticle, Journal of Materials Chemistry C 9 (2021) 5217–5226.
[34] L. Wang, D. Wang, Z. Wu, J. Luo, X. Huang, Q. Gao, X. Lai, L.-C. Tang, H. Xue, J. Gao, Self-derived superhydrophobic and multifunctional polymer sponge composite with excellent Joule heating and photothermal performance for strain/pressure sensors, ACS Appl. Mater. Interfaces 12 (11) (2020) 13316–13326.
[35] H. Lambley, T.M. Schutzius, D. Poulikakos, Superhydrophobic surfaces for extreme environmental conditions, PNAS 117 (44) (2020) 27188–27194.
[36] L.e. Ke, Y. Wang, X. Ye, W. Luo, X. Huang, B.i. Shi, Collagen-based breathable, humidity-ultrastable and degradable on-skin device, Journal of Materials Chemistry C 7 (9) (2019) 2548–2556.
[37] Y. Wang, S. Gao, W. Xu, Z. Wang, Nanogenerators with Superwetting Surfaces for Harvesting Water/Liquid Energy, Adv. Funct. Mater. 30 (2020) 1908252.
[38] T. Mouterde, P. Lecointre, G. Lehoucq, A. Checco, C. Clanet, D. Quere, Two recipes for repelling hot water, Nat. Commun. 10 (2019) 1410.
[39] T. Mouterde, G. Lehoucq, S. Xavier, A. Checco, C.T. Black, A. Rahman, T. Midavaine, C. Clanet, D. Quere, Antifogging abilities of model nanotextures, Nat. Mater. 16 (2017) 658.
[40] E. Mitridis, H. Lambley, S. Trober, T.M. Schutzius, D. Poulikakos, Transparent Photothermal Metasurfaces Amplifying Superhydrophobicity by Absorbing Sunlight Antifogging abilities of model nanotextures, ACS Nano 14 (2020) 11712.
[41] D. Zhang, S. Xu, X. Zhao, W. Qian, R. Bowen, Y. Yang, Wireless Monitoring of Small Strains in Intelligent Robots via a Joule Heating Effect in Stretchable Graphene-Polymer Nanocomposites, Adv. Funct. Mater. 30 (2020) 1910809.
[42] Y. Huang, L. Tao, J. Yu, Z. Wang, C. Zhu, X. Chen, Integrated Sensing and Warning Multifunctional Devices Based on the Combined Mechanical and Thermal Effect of Porous Graphene, ACS Appl Mater Interfaces 12 (2020) 53049–53057.
[43] C. Ma, Q. Yuan, H. Du, M. Ma, C. Si, P. Wan, Multiresponsive MXene ($Ti_3C_2T_x$)-Decorated Textiles for Wearable Thermal Management and Human Motion Monitoring, ACS Appl Mater Interfaces 12 (2020) 34226–34234.
[44] Y. Ding, T. Xu, O. Onyilagha, H. Fong, Z. Zhu, Recent Advances in Flexible and Wearable Pressure Sensors Based on Piezoresistive 3D Monolithic Conductive Sponges, ACS Appl Mater Interfaces 11 (2019) 6685–6704.
[45] M. Alhabeb, K. Maleski, B. Anasori, P. Lelyukh, L. Clark, S. Sin, Y. Gogotsi, Guidelines for Synthesis and Processing of Two-Dimensional Titanium Carbide ($Ti_3C_2T_x$ MXene), Chemistry of Materials 29 (2017) 7633–7644.
[46] L. Liu, Z. Jiao, J. Zhang, Y. Wang, C. Zhang, X. Meng, X. Jiang, S. Niu, Z. Han, L. Ren Bioinspired, Superhydrophobic, and Paper-Based Strain Sensors for Wearable and Underwater Applications. ACS Appl Mater Interfaces, 13 (2021) 1967-1978.
[47] F. Shahzad, M. Alhabeb, C.B. Hatter, B. Anasori, S. Man Hong, C.M. Koo, Y. Gogotsi, Electromagnetic interference shielding with 2D transition metal carbides (MXenes), Science 353 (2016) 1137.
[48] S. Wan, X. Li, Y. Wang, Y. Chen, X. Xie, R. Yang, A. Tomsia, L. Jiang, Q. Cheng, Strong sequentially bridged MXene sheets, Proc. Natl. Acad. Sci. U S A 117 (2020) 27154–27161.
[49] J. Luo, J. Zheng, J. Nai, C. Jin, H. Yuan, O. Sheng, Y. Liu, R. Fang, W. Zhang, H. Huang, Y. Gan, Y. Xia, C. Liang, J. Zhang, W. Li, X. Tao, Atomic Sulfur Covalently Engineered Interlayers of Ti3C2 MXene for Ultra-Fast Sodium-Ion Storage by Enhanced Pseudocapacitance, Advanced Functional Materials 29 (10) (2019) 1808107, https://doi.org/10.1002/adfm.v29.1010.1002/adfm.201808107.
[50] L. Liu, Z. Jiao, J. Zhang, Y. Wang, C. Zhang, X. Meng, X. Jiang, S. Niu, Z. Han, L. Ren Bioinspired, Superhydrophobic, and Paper-Based Strain Sensors for Wearable and Underwater Applications. ACS Appl Mater Interfaces, 13 (2021) 1967-1978.
[51] Y. Liu, H. Fan, K. Li, N. Zhao, S. Chen, Y. Ma, X. Ouyang, X. Wang, Strain-isolation bridge structure to improve stretchability of highly sensitive strain sensors, Adv. Mater. Technol. 4 (2019) 1900309.
[52] S. Zhang, H. Liu, S. Yang, X. Shi, D. Zhang, C. Shan, L. Mi, C. Liu, C. Shen, Z. Guo, Ultrasensitive and Highly Compressible Piezoresistive Sensor Based on Polyurethane Sponge Coated with a Cracked Cellulose Nanofibril/Silver Nanowire Layer, ACS Appl Mater Interfaces 11 (2019) 10922–10932.
[53] R. Xu, K. Zhang, X. Xu, M. He, F. Lu, B. Su, Superhydrophobic WS_2-Nanosheet-Wrapped Sponges for Underwater Detection of Tiny Vibration, Adv Sci (Weinh) 5 (2018) 1700655.
[54] S. Xu, X. Li, G. Sui, R. Du, Q. Zhang, Q. Fu, Plasma modification of PU foam for piezoresistive sensor with high sensitivity, mechanical properties and long-term stability, Chemical Engineering Journal 381 (2020), 122666.
[55] W. Zhai, Q. Xia, K. Zhou, X. Yue, M. Ren, G. Zheng, K. Dai, C. Liu, C. Shen, Multifunctional flexible carbon black/polydimethylsiloxane piezoresistive sensor with ultrahigh linear range, excellent durability and oil/water separation capability, Chemical Engineering Journal 372 (2019) 373–382.
[56] Y. Yue, N. Liu, W. Liu, M. Li, Y. Ma, C. Luo, S. Wang, J. Rao, X. Hu, J. Su, Z. Zhang, Q. Huang, Y. Gao, 3D hybrid porous Mxene-sponge network and its application in piezoresistive sensor, Nano Energy 50 (2018) 79–87.
[57] G. Fang, W. Li, X. Wang, G. Qiao, Droplet Motion on Designed Microtextured Superhydrophobic Surfaces with Tunable Wettability, Langmuir 24 (2008) 11651–11660.
[58] W. Li, A. Amirfazli, Microtextured superhydrophobic surfaces: a thermodynamic analysis, Adv. Colloid Interface Sci. 132 (2) (2007) 51–68.
[59] L. Miao, J.i. Wan, Y.u. Song, H. Guo, H. Chen, X. Cheng, H. Zhang, Skin-Inspired Humidity and Pressure Sensor with a Wrinkle-on-Sponge Structure, ACS Appl Mater Interfaces 11 (42) (2019) 39219–39227.
[60] Z. Yang, H. Li, S. Zhang, X. Lai, Xingrong Zeng, Superhydrophobic MXene@carboxylated carbon nanotubes/carboxymethyl chitosan aerogel for piezoresistive pressure sensor, Chemical Engineering Journal 425 (2021), 130462.